MATERIALS SCIENCE

In operando x-ray imaging of nanoscale devices: Composition, valence, and internal electrical fields

Andreas Johannes,[1]* Damien Salomon,[1] Gema Martinez-Criado,[1,2] Markus Glaser,[3] Alois Lugstein,[3] Carsten Ronning[4]

We introduce a method for directly imaging depletion layers in operando with elemental specificity and chemical speciation at sub–100 nm spatial resolution applicable to today's three-dimensional electronic architectures. These typically contain complex, multicomponent designs consisting of epitaxial heterostructures, buried domains, or nanostructures with different shapes and sizes. Although the variety of devices is immense, they commonly rely on carrier separation in a built-in potential induced by composition or strain gradients. To image these, we scanned a focused synchrotron x-ray nanobeam over a single semiconductor nanowire heterostructure and simultaneously measured the current through the device and the emitted characteristic x-rays as a function of the incoming hard x-ray energy. With these results, it is possible to identify the compositional and molecular structure as well as localize the electrical fields present under typical working conditions. This information allows us to draw an energy band diagram consistent with the elemental distribution and a high-resolution chemical speciation map.

INTRODUCTION

The cutting edge of semiconductor industry produces circuit features down to 14 nm in size (*1*, *2*) and pn junctions in solar cells spanning an area of several square meters (*3*). The respective devices have one thing in common: Their functionality relies on an internal field gradient, which is controlled by an external electric field (for example, in field-effect transistor devices) or statically induced by a compositional gradient (as in solar cells). Imaging both the internal electric fields and chemical composition of devices is thus an interesting prospect. Recently, electron beam–induced current measurements and Kelvin probe force microscopy have emerged as powerful tools to study the spatial variations of charge separation inside a device (*4*, *5*). Despite their strengths, there are several limitations imposed in terms of operating conditions, chemical sensitivity, energy tunability, penetration depth, as well as vacuum and sample preparation, which can be overcome using synchrotron radiation sources. Hard x-ray beams can probe deeply into inner grains embedded in materials, buried heterostructures, small particles, or nanodomains and investigate many properties simultaneously and in situ. These include the micro- and nanostructure in two (2D) and three (3D) dimensions (*6*–*8*) or the evolution of samples during processing (such as materials deposition and gas-phase chemical reactions) (*9*–*11*) or under operating conditions (for example, temperature cycling and catalytic reactions) (*12*–*14*). Because of the large penetrating power, a synchrotron beam is able to noninvasively obtain information from thick samples typically demanding little or no specimen preparation even under working conditions. The x-ray matter interaction provides several techniques, such as x-ray diffraction (XRD), x-ray fluorescence (XRF), resonant inelastic scattering (RISX), and x-ray beam–induced current (XBIC) (*15*). The latter has also been referred to historically by the more general term of photoconductivity (*16*–*18*) and has recently been applied in the context of nanowires (*19*) and planar solar cells (*20*, *21*). Together with developments in x-ray optics, third-generation synchrotron sources provide the brilliance needed to effectively focus x-rays down to the lower nanoscale (*22*). Because the interaction of x-rays with matter is highly energy-dependent around the absorption edges of the respective atoms within the sample, energy-dependent x-ray studies can be used to probe the local atomic environments in x-ray absorption near-edge structure (XANES) and extended x-ray absorption fine structure (EXAFS) (*6*). Here, we introduce a combinatory approach: an in operando x-ray investigation using XRF, XANES, and XBIC, mapped with a high spatial resolution of below 100 nm. The combination of these methods and high spatial resolution allows us to demonstrate structure-functionality relations on the nanoscale in individual nanowire heterostructures.

RESULTS

The investigated model structure is schematically shown in Fig. 1A and consists of a nanoscale axial Ga/GaAs segment embedded in a silicon nanowire with a SiO_2 shell. These nanowire heterostructures were synthesized by ion implantation and flash-lamp annealing and contacted with Ni electrodes (*23*, *24*). These structures show room temperature electroluminescence, and the electrical characteristics are likely defined by the Ga/GaAs Schottky junction, confirming that these heterostructures are applicable for optoelectronic devices. Implemented in large-scale top-down processed nanowire arrays, they form a potential building block for silicon photonics by combining the highly mismatched group IV and III–V semiconductors (*23*).

A nanofocused hard x-ray beam was scanned across one representative nanowire heterostructure device, and the characteristic XRF signals of Ni, Ga, and As were quantified. Figure 1B shows an overlay of a high-resolution SEM image with a color plot of the respective characteristic x-ray intensity mapping. The Ga/GaAs segment is localized within the Si nanowire. A normalized XRF line scan along the wire is plotted in Fig. 1C, and XRF spectra at specific locations are plotted in Fig. 1D together with the respective fits to the data (*25*).

The sum signal of (Ga + As) in the GaAs segment (highlighted in green in Fig. 1C, normalized to 1) corresponds to an atomic number density of 2.2×10^{22} cm^{-3} for pure GaAs. Thus, the normalized signal (green line) with a magnitude of about 0.02 to 0.05 in the Si nanowire core (position 2 in Fig.1, C and D) corresponds to about 4×10^{20} cm^{-3} to 1×10^{21} cm^{-3} or to a relative concentration of 0.8 to 2 atomic % Ga and As atoms inside Si. Here, we assumed that the nanowire diameter is

[1]European Synchrotron Radiation Facility, 71 Avenue des Martyrs, Grenoble 30843, France. [2]Instituto de Ciencia de Materiales de Madrid, Consejo Superior de Investigaciones Científicas, 28049 Cantoblanco, Spain. [3]Institute for Solid State Electronics, Technische Universität Wien, Floragasse 7, 1040 Vienna, Austria. [4]Institute of Solid State Physics, Friedrich-Schiller-University Jena, Max-Wien-Platz 1, 07743 Jena, Germany.
*Corresponding author. Email: andreas.johannes@esrf.fr

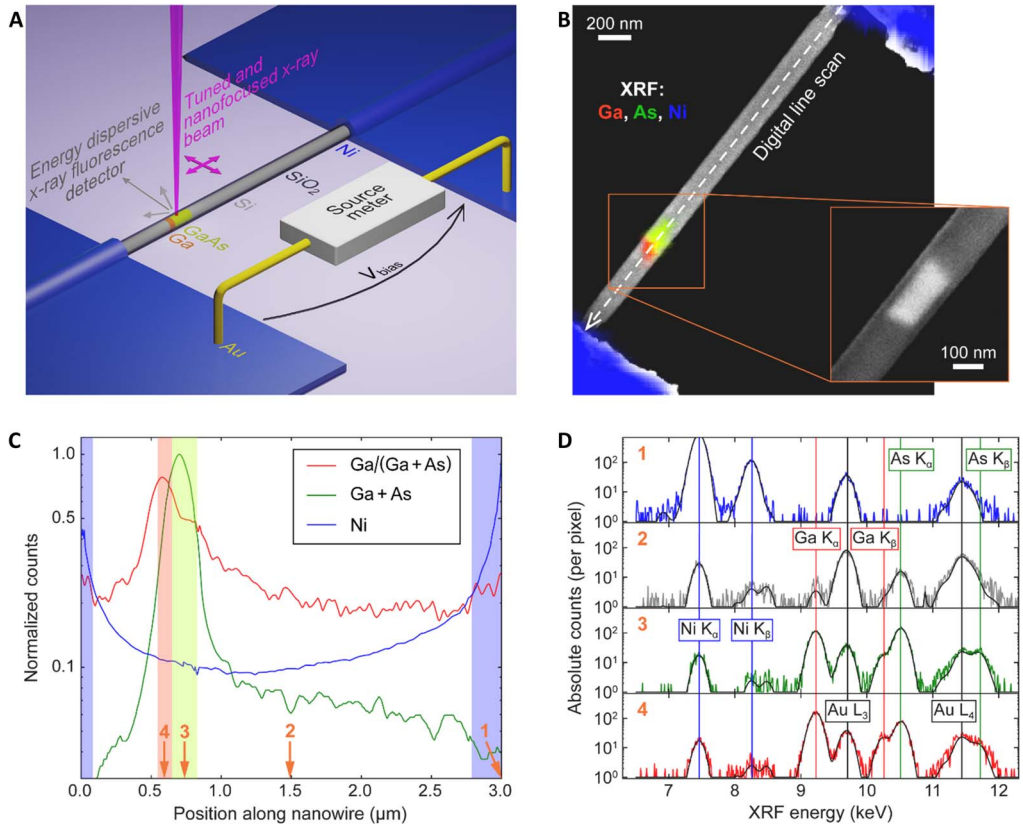

Fig. 1. Composition of the nanowire heterostructure. Composition of the nanowire heterostructure. (**A**) Schematic illustration of the device and measurement approach. (**B**) Scanning electron microscopy (SEM) image with a superimposed color plot of the Kα-XRF intensities of the heavy elements in the Si-Ga-GaAs-Si nanowire heterostructure device with Ni contacts. (**C**) Normalized XRF intensities plotted as a function of position along the wire. The Ga/(Ga + As) ratio is 0.5 at the GaAs segment (highlighted in green) and approaches 1 at one end of the GaAs segment (highlighted in red). The numbered arrows in (C) indicate the position on the nanowire axis, where the XRF spectra of single pixels shown in (**D**) were measured.

constant and thin enough to exclude self-absorption. The Ga/(Ga + As) ratio in this segment is about 0.2 (red line in Fig. 1C), which is well in line with the degenerate n-type doping found in a previous electrical study of identical structures (*23*). Finally, Fig. 1C shows that there is a segment with excess Ga at position 4, where the Ga/(Ga + As) ratio is well above 0.5, whereas the GaAs segment at position 3 has a ratio of exactly 50%. It is clear that there is only an excess of Ga at one side of the GaAs segment. These findings are in full agreement with previous transmission electron microscopy–energy-dispersive x-ray (TEM-EDX), electrical, and Raman investigations of these nanowire heterostructure devices (*23*). The artefact Au signal in all spectra (Fig. 1D) stems from gold bond wires connected to the Ni electrodes, which were excited by x-rays scattered in the substrate. Because the XRF signal was always measured in parallel with the electrical characteristics, it was possible to correct subsequent mappings online for any lateral sample drift (*26*). This live correction and a similar post-measurement correction ensure that all the following results have a high positional accuracy of about 30 nm.

Figure 2A shows the 2D maps of the Ga/(Ga + As) ratio, the normalized XRF signal of (Ga + As), and the x-ray nanobeam excited current (XBIC) measured at −0.7-V bias. All signals were normalized to 1 for this illustration. Figure 2B shows the extracted signals plotted as a function of the position along the nanowire. This simultaneous measurement of the XBIC with XRF allows the unambiguous localization of the active area of the device on a nanometer scale: It is at the interface between the Ga segment (red background, highest Ga concentration) and the GaAs segment [green background, Ga/(Ga + As) ≈ 0.5]. The typical Schottky diode–like *I*-*V* curves of this device are thus confirmed to be defined by the metal/semiconductor (that is, Ga/GaAs junction).

In Fig. 2C, the *I*-*V* characteristics of the nanowire heterostructure are shown for the case of the x-ray nanobeam focused on the active area of the device (red circles) and for dark conditions without x-ray irradiation (black circles). A clear change in sensitivity with applied bias can be deduced from the logarithmic plot (top). For moderate positive voltages and large negative voltages, there is a large current flowing continuously through the device, almost independent on the presence of the x-ray beam. A high sensitivity of two orders of magnitude is found at a moderate reverse bias of about −0.7 V. Note that the difference between the dark current and the XBIC at 4 V applied bias is about 1 μA, whereas at the point of highest sensitivity, the x-rays only induce an additional current of about 1 nA. Because both values were measured under the same excitation condition, this indicates that a strong, bias-dependent, charge amplification process is present. This is most likely due to impact ionization in the reverse breakdown regime and will be discussed below.

In addition to the XRF and XBIC measurements with a fixed incoming x-ray energy of 29.33 keV, a series of maps on the same nanowire structure were recorded with varying x-ray energies around the Ga-K absorption edge. XANES spectra were extracted from these maps and are plotted in Fig. 3A for the positions 1 to 10 along the

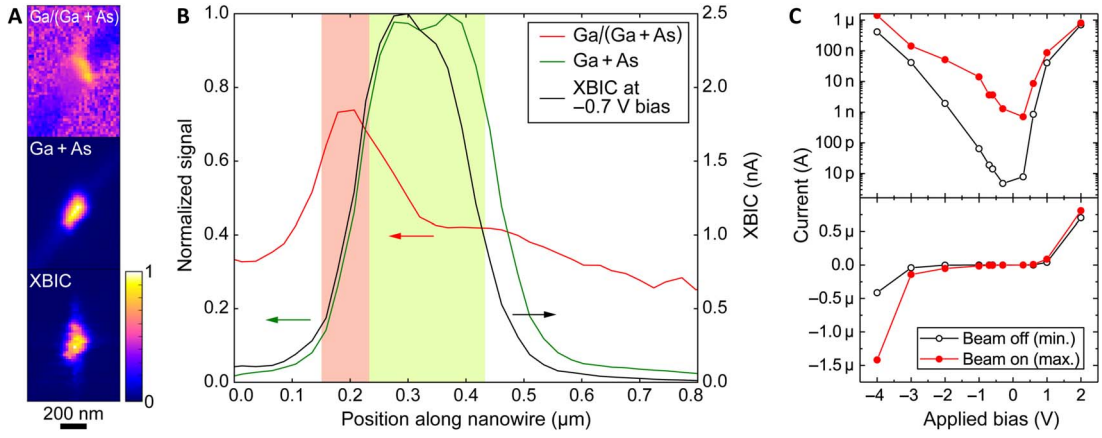

Fig. 2. Simultaneous XRF and XBIC recording. (**A**) 2D mapping of the Ga/(Ga + As) ratio, normalized XRF signal of (Ga + As), and XBIC at −0.7-V bias; each pixel is 20 × 20 nm^2. In the line scan (**B**) extracted from the maps, the colored background indicates the Si (white), Ga (red), and GaAs (green) sections of the heterostructure as identified by XRF. (**C**) *I-V* characteristics of this device in logarithmic (top) and linear scale (bottom). The black hollow circles show the current without x-ray nanobeam (that is, dark conditions), whereas the red filled circles represent the maximum current found when the x-ray nanobeam was focused on the active area of the device.

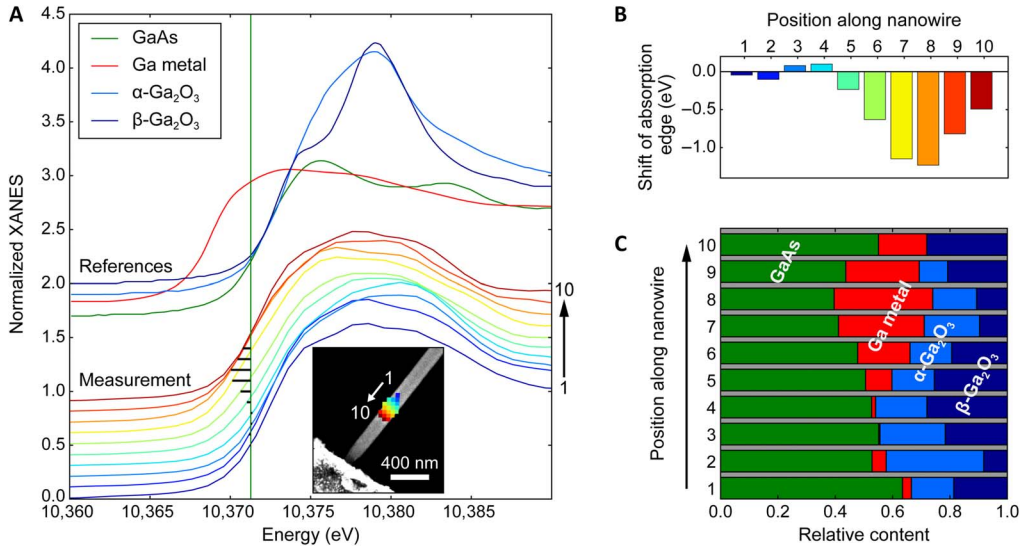

Fig. 3. Position-resolved Ga-edge XANES spectra measured on a nanoscale along the nanowire heterostructure. (**A**) The lower group of spectra (1 blue→10 red) shows the normalized, averaged data offset according to their position along the nanowire. The top four graphs (green, red, blue, and dark blue) show the spectra of reference materials, as indicated in the legend (*6*, *27*). The inset SEM image is overlaid with a color plot indicating the points from which the respective XANES spectra (1 to 10) were extracted. The green vertical line indicates the absorption edge of Ga in GaAs. Relative to this line, the black horizontal lines and the bar graph in (**B**) indicate the shift of the measured absorption edge as a function of the position along the nanowire. (**C**) Normalized fractions of a linear combination analysis of the measured XANES spectra using the reference materials.

nanowire axis, as shown in the inset of Fig. 3A. The energetic position of the XANES absorption edge is mainly given by the valence state of the absorbing atom. This can be seen in the reference spectra, also plotted in Fig. 3A, where the absorption edge of metallic Ga is shifted to lower energies compared to the absorption edge of the gallium oxides or GaAs (*6*, *27*). The features on the high-energy side of the absorption edge can be used to tentatively identify the coordination number of the absorbing Ga atom by comparison to known coordinations (*28*). The first peak at 10,372 eV is most pronounced in GaAs and is attributed to a tetrahedral coordination, whereas the peak at 10,376 eV is more pronounced in the β-Ga_2O_3 phase and attributed to octahedrally coordinated Ga. Because each Ga atom in the material absorbs x-rays incoherently, a measured XANES spectrum corresponds to the linear combination of the spectra of all configurations present in the given excitation volume.

The main phases very likely to be present in this heterostructure are GaAs and Ga-metal (liquid or solid). In addition, there will be a hardly definable combination of Ga in a covalent matrix with Si and O from the Si nanowire and SiO_2 shell. The first reference material, GaAs (*6*), is plotted in green in Fig. 3A. To confirm the energy calibration, a GaAs wafer was also measured, with our setup giving essentially the same spectrum (see the Supplementary Materials). The Ga metal K-edge absorption spectrum shown in red in Fig. 3A was taken from the study of Armbrüster and Cardoso-Gil (*27*). It is possible to distinguish supercooled liquid from solid metallic Ga in XANES (*29*), but the respective features are in the post-edge region, where we observe a large

contribution of the GaAs signal. Therefore, the difference between XANES of liquid and solid Ga is too subtle to be evident in our data. Because the whole nanowire was covered with an SiO_2 shell during the formation of the heterostructure by applying high-temperature flash annealing procedures (*23*), gallium oxide phases are assumed to form in the vicinity of the core-shell interface by consuming Ga and oxygen atoms from the Ga/GaAs segments and the SiO_2 shell, respectively. The contribution of these Ga atoms is roughly modeled as an arbitrary combination of tetrahedrally and octahedrally coordinated Ga atoms, α- and β-Ga_2O_3. It should be noted that because of the possible presence of unaccounted gallium silicate phases, this does not imply an observation of the metastable α-Ga_2O_3 phase, although its presence cannot be categorically excluded either (*6*). Both Ga_2O_3 spectra were also taken from the study of Martínez-Criado *et al.* (*6*); the energy axes for the references and measured spectra were mutually aligned (see the Supplementary Materials).

Figure 3C shows the results of the linear combination fit of the indicated reference spectra to the measured data (for more details, see the Supplementary Materials). The main contribution to the XANES spectrum is GaAs, as expected from the XRF data. There is a varying contribution of the octahedrally and tetrahedrally coordinated Ga, as unspecifically modeled by α- and β-Ga_2O_3. The shift of the absorption edge to lower energies by more than 1 eV in spectra 6 to 10, shown in Fig. 3B, can be obviously modeled by the presence of metallic Ga. Because there is no other method of significantly decreasing the energy of the absorption edge, this finding is unambiguously related to the unoxidized, metallic Ga. This conclusion is highly reliable, because each spatial map was fully measured before the x-ray energy was changed and, therefore, the relative shift as a function of position on the sample is totally unaffected by potential inaccuracies of the incoming x-ray energy caused by the beamline monochromator.

In parallel to the XRF measurements, the XBIC signal was recorded as a function of the monochromatic x-ray energy. Figure 4A shows the measured current together with the Ga-K series XRF measured at the position of the Ga segment indicated with a black square in the inset of Fig. 4A. The blue curve shows the unstandardized current, and a large XBIC signal is already present for incoming x-ray energies lower than the Ga-K absorption edge, followed by a distinct increase by a factor of 2 when the x-ray energy exceeds the Ga core-level energy. This unambiguously shows that K-shell electrons of Ga are excited to the conduction band and that this core excitation contributes significantly to the device conductivity.

DISCUSSION

As schematically shown in Fig. 4B, for the present materials and at an x-ray energy of about 10 keV, the dominating processes are photoionization of Ga and As (see the Supplementary Materials for details). For energies below the Ga-K edge, these are restricted to excitations of the L-shell, for which the cross section varies little with the incoming x-ray energy. The main energy dependence observed in the measured XBIC signal is caused by the significant contribution of excited electrons out of the Ga K-shell when an incoming x-ray photon has a sufficiently large energy to ionize it. This is also the process that causes the XRF XANES signal, because XRF photons are generated only when the localized core-level vacancy is radiatively filled by an electron from the surrounding material, usually from the same atom. Thus, the energy dependences of the characteristic Ga K-series XRF and the XBIC have the same physical origin in the photoionization cross section of Ga atoms in their respective local environments.

There is a useful difference between XBIC and XRF XANES, however, because the former is position-selective only to those charge carriers that are separated and thus to the functional area of the investigated device. On the other hand, the characteristic XRF signal includes all the atoms of a species within the excited volume (*17*). Using the high spatial resolution of this experiment, we can show this difference in the inset of Fig. 4A, which shows an SEM image of the device overlaid with the total XRF signal (left) and the XBIC signal (right), both measured at the same time. The whole Ga-containing segment yields large XRF signals that are offset from the background. However, the largest XBIC signal is highly localized at the interface of the metallic Ga and GaAs segments. Thus, this can be identified as the depletion zone of the Schottky contact, extending into the GaAs segment. Free charge carriers are generated in the depletion zone after excitation by x-ray photons and are separated by the large electric field gradients to contribute to the measured XBIC. It is noteworthy that there is also a large halo around the charge-separating interface only for the XBIC signal and not for the XRF, although both the XRF and the XBIC color overlays use the same linear color map. The halo corresponds to the side lobes of the (invariably imperfectly) focused

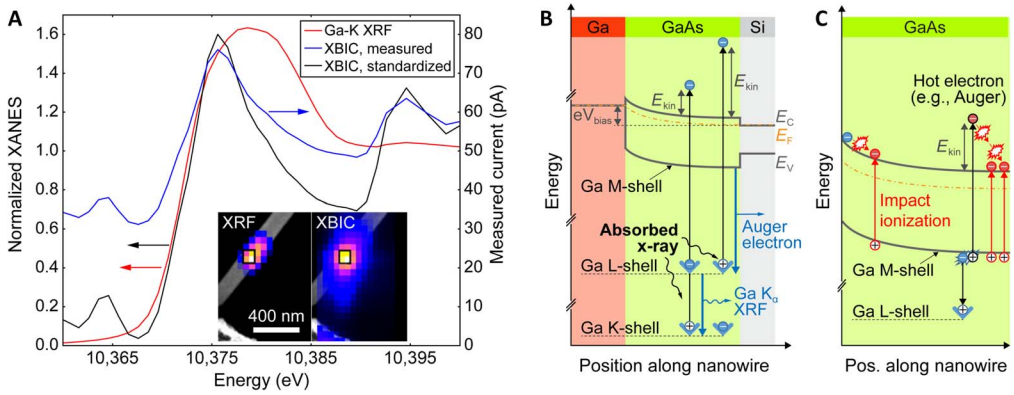

Fig. 4. Energy-dependent XBIC analysis. (**A**) Simultaneously recorded Ga XRF (red) and XBIC (black, standardized; blue, as measured) signals as a function of x-ray energy. The insets show an SEM image overlaid with the map of the sum of the respective signal for all energies. The black square in the inset maps indicated the four pixels averaged to give the plotted spectra. (**B**) Band diagram showing the principal excitation mechanisms of absorption and inelastic scattering. (**C**) Main charge amplification process of impact ionization. Note that the de-excitation cascade of a single absorption event leads to a large number of charge carriers.

nanobeam, and the fact that it is detectable in the XBIC signal highlights its high sensitivity in this reverse bias regime. Finally, a current signal is also detected when the incoming x-rays hit the Ni contacts. Here, the current is induced by removing photoelectrons from the contact. Because the nanowire heterostructure acts as a rectifier, the photoelectron current at each electrode changes sign with the bias voltage.

This leads us to a further discussion of the underlying mechanism for XBIC. First, as already mentioned, photoionization of the Ga and As L-shell also contributes to the signal. As in any measurement method for XANES, this could be taken into account and removed; however, the relatively large and constant current induced by this absorption reduces the effective signal-to-noise ratio. The large sensitivity of the XBIC, as seen in the halo in the inset of Fig. 4A, is caused by the efficient conversion of a single absorbed photon into thousands of mobile charge carriers. This is illustrated schematically in Fig. 4C. In either case of a K- or L-shell absorption event, the primary and secondary (Auger) electrons will generally have ample kinetic energy, that is, they will be "hot". Similar to electrons accelerated in the applied or internal electric field, they can therefore excite further electrons from the valence band or defect levels to the conduction band. On top of this, for all charge carriers, a high externally applied bias and internal electric field can lead to impact ionization cascades. This secondary charge amplification is also responsible for the bias-dependent sensitivity of the device seen in the *I-V* characteristics (Fig. 3C).

It may be tempting to read more into the post-absorption edge features found in the XBIC-XANES of Fig. 4A. A hypothesis could be that a strong energy dependence of the number of additional electron-hole pairs each hot electron creates may translate into additional features in the post-edge region. These features would be related to the density of states, as in x-ray photoelectron spectroscopy (XPS). In large-beam experiments, similar ideas have been published (*30*–*32*); however, they are heavily contested (*16*). The convincing counter-argument is that the large multiplication factor together with the multitude of de-excitation paths for each absorbed x-ray photon statistically negates the difference in the mean number of excited charge carriers between two impinging x-ray photons of differing energy, except for a linear relation to the impinging photon energy. Therefore, in a previously published XBIC study, then called photoconductivity, x-ray absorption spectroscopy (XAS) studies on GaAs have failed to show any difference between photoconductivity, absorption, or fluorescence XAS spectra (*16*–*18*). The post-absorption edge features remain those given by the fine structure of the absorption cross section, without an "anomalous" contribution by energetic delocalized electrons. Within the experimental accuracy obtained in our experiment, this conclusion can be supported.

This in operando analysis of a functional nanoscale heterojunction demonstrates the added value of a combinatory study using focused x-rays. Here, we made particular use of the possibility to change the x-ray energy to obtain information on the composition and chemical bonding of the materials present in the heterostructure. Together with the measurement of an operative characteristic in the conductivity, we can unambiguously identify that there is a metallic Ga segment in the heterostructure and that the Ge-GaAs interface is the active part of the Si-Ga-GaAs-Si heterostructure. In this scenario, we did not yet take full advantage of the high penetration depth of x-rays, or of the ability to work under other than ambient conditions, so that this method is set to open further horizons. The high penetration power combined with the localized XBIC probe will be useful for the detailed investigation of the mechanism of buried junctions/devices without destroying them, such as the planar junctions in solar cells. In addition, it is possible to perform such studies in temperature-controlled and chemically controlled environments (for example, on catalysts in a reactor).

MATERIALS AND METHODS

Nanowire heterostructure synthesis

All simultaneously measured XRF, XANES, and XBIC data presented in this work were taken from one single Si-Ga-GaAs-Si nanowire heterostructure. This structure was synthesized by Ga^+ and As^+ ion irradiation into vapor-liquid-solid–grown Si nanowires (*33*), which was covered by plasma-enhanced chemical vapor deposition with SiO_2. A subsequent flash-lamp annealing step leads to the heterostructure formation via liquid-phase epitaxy within the wire. All synthesis details are reported by Glaser *et al.* (*23*). The electrical contacts were deposited by standard e-beam lithography, Ni sputter deposition, and lift-off techniques, including a hydrofluoric acid etching step to remove the SiO_2 shell from the nanowires at the contact area for reliable contact formations.

X-ray nanoprobe investigation

The x-ray investigations were performed at the nano-analysis beamline ID16B of the European Synchrotron Radiation Facility (*34*). The data for the XRF quantification and some of the XBIC measurements were performed at 29.33 keV in "pink-beam" mode with an average flux of 1.4×10^{11} photons/s and a focal spot size of 40 nm × 50 nm. The step size for the spatial maps was 20 nm. The XANES investigations were performed with a monochromatic nanobeam at an energy bandwidth of 1 eV. Here, the photon flux was 2.35×10^8 photons/s with a focal spot of 90 nm × 80 nm. See the Supplementary Materials for more details on the beam size. The energy steps were varied between 1 and 5 eV to cover the Ga absorption edge. At each energy, a special mapping of about 1 μm × 3 μm was performed. To correct for sample drift, the position of the sample was corrected using an image alignment procedure (*26*). One energy scan was performed with 50-nm steps and 200-ms exposure time, whereas the second scan was performed with 30-nm steps and 400-ms exposure time. During all measurements, an electric source measurement unit (Stanford Research System SR570) was connected to the sample to measure the current induced by the x-ray nanobeam. The XBIC signal was acquired as a function of bias voltage (Fig. 2C) and incoming x-ray photon energy (Fig. 4A) at a fixed bias of −0.3 V.

SUPPLEMENTARY MATERIALS

Supplementary material for this article is available at http://advances.sciencemag.org/cgi/content/full/3/12/eaao4044/DC1

Detailed description of XANES mapping
Standard XANES data treatment
Discussion of energy calibration
Discussion of x-ray–matter interaction with respect to XBIC yield
Discussion of the spatial resolution
fig. S1. Ga in Ga_2O_3 K-edge XANES references.
fig. S2. Ga in GaAs K-edge XANES.
fig. S3. Linear combination analysis of XRF data.
fig. S4. Linear combination analysis of XBIC data.
fig. S5. Determination of the spatial resolution of the setup.
table S1. XANES energy steps of the x-ray beam for the XANES measurements.
table S2. Cross sections and Auger yields for relevant elements and x-ray energies.
References (*35*–*42*)

REFERENCES AND NOTES

1. J.-A. Carballo, W.-T. J. Chan, P. A. Gargini, A. B. Kahng, S. Nath, ITRS 2.0: Toward a re-framing of the Semiconductor Technology Roadmap, *2014 32nd IEEE International Conference on Computer Design (ICCD)*, Seoul, South Korea, 19 to 22 October 2014 (IEEE, 2014).

2. A. Kaneko, A. Yagishita, K. Yahashi, T. Kubota, M. Omura, K. Matsuo, I. Mizushima, K. Okano, H. Kawasaki, S. Inaba, T. Izumida, T. Kanemura, N. Aoki, K. Ishimaru, H. Ishiuchi, K. Suguro, K. Eguchi, Y. Tsunashima, Sidewall transfer process and selective gate sidewall spacer formation technology for sub-15nm FinFET with elevated source/drain extension, *IEEE International Electron Devices Meeting, 2005. IEDM Technical Digest*, Washington, DC, 5 December 2005 (IEEE, 2005).
3. M. A. Green, K. Emery, Y. Hishikawa, W. Warta, E. D. Dunlop, Solar cell efficiency tables (version 45). *Prog. Photovolt. Res. Appl.* **23**, 1–9 (2015).
4. H. Harada, A. Onoda, S. Moriguchi, T. Hayashi, In situ observation of enhanced photoinduced charge separation in a gold nanoparticle assembly immobilized on TiO_2. *ChemistrySelect* **1**, 5666–5670 (2016).
5. G. Seo, D. Lee, S. Heo, M. Seol, Y. Lee, K. Kim, S. H. Kim, J. Lee, D. Lee, J. Lee, D. W. Kwak, D. Lee, H. Y. Cho, J. Park, T. K. Ahn, M. K. Nazeeruddin, Microscopic analysis of inherent void passivation in perovskite solar cells. *ACS Energy Lett.* **2**, 1705–1710 (2017).
6. G. Martínez-Criado, J. Segura-Ruiz, M.-H. Chu, R. Tucoulou, I. López, E. Nogales, B. Mendez, J. Piqueras, Crossed Ga_2O_3/SnO_2 multiwire architecture: A local structure study with nanometer resolution. *Nano Lett.* **14**, 5479–5487 (2014).
7. J. Wallentin, M. Osterhoff, T. Salditt, In operando x-ray nanodiffraction reveals electrically induced bending and lattice contraction in a single nanowire device. *Adv. Mater.* **28**, 1788–1792 (2016).
8. M. Holler, M. Guizar-Sicairos, E. H. R. Tsai, R. Dinapoli, E. Müller, O. Bunk, J. Raabe, G. Aeppli, High-resolution non-destructive three-dimensional imaging of integrated circuits. *Nature* **543**, 402–406 (2017).
9. J. W. Gallaway, A. M. Gaikwad, B. Hertzberg, C. K. Erdonmez, Y.-C. K. Chen-Wiegart, L. A. Sviridov, K. Evans-Lutterodt, J. Wang, S. Banerjee, D. A. Steingart, An in situ synchrotron study of zinc anode planarization by a bismuth additive. *J. Electrochem. Soc.* **161**, A275–A284 (2013).
10. S. Kowarik, Thin film growth studies using time-resolved x-ray scattering. *J. Phys. Condens. Matter* **29**, 043003 (2017).
11. J. Dendooven, E. Solano, M. M. Minjauw, K. Van de Kerckhove, A. Coati, E. Fonda, G. Portale, Y. Garreau, C. Detavernier, Mobile setup for synchrotron based in situ characterization during thermal and plasma-enhanced atomic layer deposition. *Rev. Sci. Instrum.* **87**, 113905 (2016).
12. C. Zhao, K. Fezzaa, R. W. Cunningham, H. Wen, F. De Carlo, L. Chen, A. D. Rollett, T. Sun, Real-time monitoring of laser powder bed fusion process using high-speed X-ray imaging and diffraction. *Sci. Rep.* **7**, 3602 (2017).
13. J. Villanova, R. Daudin, P. Lhuissier, D. Jauffrès, S. Lou, C. L. Martin, S. Labouré, R. Tucoulou, G. Martínez-Criado, L. Salvo, Fast in situ 3D nanoimaging: A new tool for dynamic characterization in materials science. *Mater. Today* **20**, 354–359 (2017).
14. S. W. T. Price, D. J. Martin, A. D. Parsons, W. A. Sławiński, A. Vamvakeros, S. J. Keylock, A. M. Beale, J. F. W. Mosselmans, Chemical imaging of Fischer-Tropsch catalysts under operating conditions. *Sci. Adv.* **3**, e1602838 (2017).
15. S. Amelinckx, D. van Dyck, J. van Landuyt, G. van Tendeloo, Eds., *Handbook of Microscopy* (Wiley-VCH Verlag GmbH, 1996).
16. J. Bollmann, S. Knack, J. Weber, V. Koteski, H.-E. Mahnke, E. Welter,Limitations of electrical detection of x-ray absorption fine structure. *Phys. Rev. B* **68**, 125206 (2003).
17. R. F. Boehme, G. S. Cargill III, W. Weber, T. Jackson, Diode current detection of extended x-ray absorption fine structure in gallium arsenide. *J. Appl. Phys.* **58**, 811–815 (1985).
18. T. D. Hu, Y. N. Xie, S. Qiao, Y. Hai, Y. L. Jin, D. C. Xian, Photoconduction extended x-ray-absorption fine structure of GaAs. *Phys. Rev. B.* **50**, 2216–2220 (1994).
19. J. Wallentin, M. Osterhoff, R. N. Wilke, K.-M. Persson, L.-E. Wernersson, M. Sprung, T. Salditt, Hard x-ray detection using a single nm diameter nanowire. *Nano Lett.* **14**, 7071–7076 (2014).
20. M. Stuckelberger, T. Nietzold, G. N. Hall, B. West, J. Werner, B. Niesen, C. Ballif, V. Rose, D. P. Fenning, M. I. Bertoni, Charge collection in hybrid perovskite solar cells: Relation to the nanoscale elemental distribution. *IEEE J. Photovolt.* **7**, 590–597 (2017).
21. M. Stuckelberger, B. West, T. Nietzold, B. Lai, J. M. Maser, V. Rose, M. I. Bertoni, Engineering solar cells based on correlative X-ray microscopy. *J. Mater. Res.* 1–30 (2017).
22. A. Somogyi, C. Mocuta, Possibilities and challenges of scanning hard x-ray spectro-microscopy techniques in material sciences. *AIMS Mater. Sci.* **2**, 122–162 (2015).
23. M. Glaser, A. Kitzler, A. Johannes, S. Prucnal, H. Potts, S. Conesa-Boj, L. Filipovic, H. Kosina, W. Skorupa, E. Bertagnolli, C. Ronning, A. Fontcuberta i Morral, A. Lugstein, Synthesis, morphological, and electro-optical characterizations of metal/semiconductor nanowire heterostructures. *Nano Lett.* **16**, 3507–3513 (2016).
24. S. Prucnal, M. Glaser, A. Lugstein, E. Bertagnolli, M. Stöger-Pollach, S. Zhou, M. Helm, D. Reichel, L. Rebohle, M. Turek, J. Zuk, W. Skorupa, III–V semiconductor nanocrystal formation in silicon nanowires via liquid-phase epitaxy. *Nano Res.* **7**, 1769–1776 (2014).
25. V. A. Solé, E. Papillon, M. Cotte, P. Walter, J. Susini, A multiplatform code for the analysis of energy-dispersive X-ray fluorescence spectra. *Spectrochim. Acta Part B* **62**, 63–68 (2007).
26. M. Cotte, E. Pouyet, M. Salomé, C. Rivard, W. De Nolf, H. Castillo-Michel, T. Fabris, L. Monico, K. Janssens, T. Wang, P. Sciau, L. Verger, L. Cormier, O. Dargaud, E. Brun, D. Bugnazet, B. Fayard, B. Hesse, A. E. Pradas del Real, G. Veronesi, J. Langlois, N. Balcar, Y. Vandenberghe, V. Armando Solé, J. Kieffer, R. Barrett, C. Cohen, C. Cornu, R. Baker, E. Gagliardini, E. Papillon, J. Susini, The ID21 X-ray and infrared microscopy beamline at the ESRF: Status and recent applications to artistic materials. *J. Anal. At. Spectrom.* **32**, 477–493 (2017).
27. M. Armbrüster, R. Cardoso-Gil, Synthesis of supported Ga nanodrops by a bottom-up route: Synthesis of supported Ga nanodrops by a bottom-up route. *Z. Anorg. Allg. Chem.* **641**, 1453–1458 (2015).
28. C. Revenant, M. Benwadih, O. Proux, Local structure around Zn and Ga in solution-processed In–Ga–Zn–O and implications for electronic properties. *Phys. Status Solidi RRL* **9**, 652–655 (2015).
29. G. B. Parravicini, A. Stella, Extreme undercooling (down to 90 K) of liquid metal nanoparticles. *Appl. Phys. Lett.* **89**, 033123 (2006).
30. M. Ishii, Site-specific x-ray absorption spectroscopy of electron traps by x-ray-induced displacement current measurement. *Phys. Rev. B* **65**, 085310 (2002).
31. M. Ishii, T. Uchihashi, X-ray absorption measurement by scanning capacitance microscopy. *Phys. B Condens. Matter* **340–342**, 1142–1146 (2003).
32. M. Ishii, Y. Yoshino, K.-i. Takarabe, O. Shimomura, Direct observation of local structure of DX center by capacitance X-ray absorption fine structure. *Phys. B Condens. Matter* **273–274**, 774–777 (1999).
33. R. Wagner, W. Ellis, Vapor-liquid-solid mechanism of single crystal growth. *Appl. Phys. Lett.* **4**, 89 (1964).
34. G. Martínez-Criado, J. Villanova, R. Tucoulou, D. Salomon, J.-P. Suuronen, S. Labouré, C. Guilloud, V. Valls, R. Barrett, E. Gagliardini, Y. Dabin, R. Baker, S. Bohic, C. Cohen, J. Morse, ID16B: A hard X-ray nanoprobe beamline at the ESRF for nano-analysis. *J. Synchrotron Radiat.* **23**, 344–352 (2016).
35. G. Bunker, *Introduction to XAFS: A Practical Guide to X-Ray Absorption Fine Structure Spectroscopy* (Cambridge Univ. Press, 2010).
36. K. Nishi, K.-i. Shimizu, M. Takamatsu, H. Yoshida, A. Satsuma, T. Tanaka, S. Yoshida, T. Hattori, Deconvolution analysis of Ga K-Edge XANES for quantification of gallium coordinations in oxide environments. *J. Phys. Chem. B* **102**, 10190–10195 (1998).
37. A.-C. Wei, P.-H. Liu, K.-J. Chao, E. Yang, H.-Y. Cheng, X-ray absorption measurement and density functional theory analysis of gallium in gallium-containing beta zeolites. *Microporous Mesoporous Mater.* **47**, 147–156 (2001).
38. T. Schoonjans, A. Brunetti, B. Golosio, M. Sanchez del Rio, V. A. Solé, C. Ferrero, L. Vincze, The xraylib library for X-ray–matter interactions. Recent developments. *Spectrochim. Acta Part B* **66**, 776–784 (2011).
39. A. Brunetti, M. Sanchez del Rio, B. Golosio, A. Simionovici, A. Somogyi, A library for X-ray–matter interaction cross sections for X-ray fluorescence applications. *Spectrochim. Acta Part B* **59**, 1725–1731 (2004).
40. O. Demichel, M. Heiss, J. Bleuse, H. Mariette, A. Fontcuberta i Morral, Impact of surfaces on the optical properties of GaAs nanowires. *Appl. Phys. Lett.* **97**, 201907 (2010).
41. S. Breuer, C. Pfüller, T. Flissikowski, O. Brandt, H. T. Grahn, L. Geelhaar, H. Riechert, Suitability of Au- and self-assisted GaAs nanowires for optoelectronic applications. *Nano Lett.* **11**, 1276–1279 (2011).
42. C. Gutsche, R. Niepelt, M. Gnauck, A. Lysov, W. Prost, C. Ronning, F.-J. Tegude, Direct determination of minority carrier diffusion lengths at axial GaAs nanowire p–n junctions. *Nano Lett.* **12**, 1453–1458 (2012).

Acknowledgments: We acknowledge the great work done by the past and present staff at ID16B in building a beamline which makes these experiments possible. We thank W. de Nolf for making the image alignment software "spectrocrunch" available. We also thank the European Synchrotron Radiation Facility (ESRF) for the beam time allocated. **Funding:** We acknowledge financial support by the Deutsche Forschungsgemeinschaft (DFG; RO 1198/14-1) and Austrian Science Fund (FWF; No. I 724-N16) under the auspices of the D-A-CH-project "Wiring quantum dots," the German Ministry for Research and Technology (BMBF) within the project "nano@work" (05K16SJ1), and the ESRF for the allocated beam time. G.M.-C. thanks the partial financial support from Consejo Superior de Investigaciones Científicas through the project 201660I001.
Author contributions: M.G., A.J., C.R., and A.L. conceived and performed the nanowire heterostructure synthesis, contacting, and first characterization. A.J., D.S., and G.M.-C. conceived and performed the x-ray measurements and analyzed the x-ray data. A.J. and C.R. wrote the paper with input from all other authors. A.J. claims responsibility for the content of all figures. **Competing interests:** The authors declare that they have no competing interests. **Data and materials availability:** All data needed to evaluate the conclusions in the paper are present in the paper and/or the Supplementary Materials. Additional data related to this paper may be requested from the authors.

Submitted 17 July 2017
Accepted 8 November 2017
Published 8 December 2017
10.1126/sciadv.aao4044

Citation: A. Johannes, D. Salomon, G. Martinez-Criado, M. Glaser, A. Lugstein, C. Ronning, In operando x-ray imaging of nanoscale devices: Composition, valence, and internal electrical fields. *Sci. Adv.* **3**, eaao4044 (2017).

In operando x-ray imaging of nanoscale devices: Composition, valence, and internal electrical fields

Andreas Johannes, Damien Salomon, Gema Martinez-Criado, Markus Glaser, Alois Lugstein and Carsten Ronning

Sci Adv **3** (12), eaao4044.
DOI: 10.1126/sciadv.aao4044